A Model for Multiview Ultrasonic Array Inspection of Small Two-Dimensional Defects

Nicolas Budyn, Rhodri L. T. Bevan, Jie Zhang, Anthony J. Croxford, and Paul D. Wilcox

***Abstract*— The multiview total focusing method (TFM) is an imaging algorithm for ultrasonic full matrix array data that exploits internal reflections and mode conversions in the inspected object to create multiple images, the views. Modeling the defect response in multiview TFM is an essential first step in developing new detection and characterization methods that exploit the information present in these views. This paper describes a ray-based forward model for small 2-D defects and compares its results against finite-element simulations and experimental data for the inspection of a side-drilled hole, a notch, and a crack. A simpler version of this model, based on a single-frequency approximation, is derived and compared. A good agreement with the multifrequency model and a speedup of several orders of magnitude are achieved.**

***Index Terms*— Acoustic propagation, array signal processing, modeling, phased arrays, ultrasonic imaging, ultrasonic transducer arrays.**

I. Introduction

ULTRASONIC arrays are commonly used in industrial nondestructive evaluation (NDE) for a wide range of applications [1]. Postprocessing the full matrix capture (FMC) data (also referred to as multistatic response matrix [2] or full array response matrix [3]), which contains the time traces corresponding to each pair of transmitter and receiver, is an active area of research. A common approach, the total focusing method (TFM) synthetically focuses the wavefront at every point of a grid to form an image [4]. The multiview TFM, also known as multimodal TFM,[1] is an extension that exploits internal reflections and mode conversions to create multiple image views from the same FMC data set [5]. Various investigations have demonstrated the suitability and the overall good performance of multiview TFM for the inspection of notches, cracks, side-drilled holes, and welds [5]–[12]. Using an amplitude drop measurement technique in multiview TFM images, accurate and reliable sizing of notches larger than two wavelengths was obtained [9], [10]. Other algorithms such as multiple signal classification (MUSIC) [13] and plane-wave imaging [14] and plane wave with phase coherence imaging [15] have also been successfully adapted to multiview imaging.

The authors are interested in data fusion across multiple TFM views to improve the detectability and characterization of defects. For the detection problem, the location of the defect (if there is one) is *a priori* unknown, so any position in any view is considered as a potential defect location. The response of a defect greatly varies with factors that include: 1) the type and size of defect; 2) the view; 3) the position of the defect within the view; and 4) the exact setup (e.g., probe position relative to the specimen, specimen geometry, specimen and couplant ultrasonic velocities, and specimen thickness). Consequently, the response of a defect may be strong in one view but weak in another, so it is necessary to determine which positions in which views are likely to contain useful information and which are not. The authors, therefore, desire a fast way of estimating the defect response at all positions in all views for a given setup.

This paper focuses on modeling the ultrasonic response of a small 2-D scatterer and in particular its maximum TFM intensities across different views. Various modeling techniques are suitable, including the finite-element method (FEM) and analytical models such as the commercial software CIVA UT [16]. The aim of the current work is to calculate the TFM intensities of small defects with an even higher computational efficiency. This is an essential first step to develop new defect detection and characterization techniques. This is done by deriving an estimator of the TFM intensities from an analytical model. First, this paper describes a frequency-domain ray-based linear time-invariant (LTI) 2-D forward model for efficiently predicting the intensity of multiview TFM images with arbitrarily shaped defects at any location. Then, the model is validated against experimental and finite-element data for a side-drilled hole, a crack, and a notch. Finally, a simpler and significantly faster single-frequency version is derived for even higher computational efficiency and is compared.

A. Inspection Configuration

The inspection configuration shown in Fig. 1(a) approximates a common NDE scenario where the fusion of multiview TFM could lead to significant improvements in automated defect detection and characterization: the inspection of the fusion face of a weld. The ultrasonic array is held at a distance from and inclined relative to the top surface of the specimen to ensure good generation of longitudinal and transverse waves. The region of interest, where defects may occur, is not directly

Manuscript received December 14, 2018; accepted March 15, 2019. Date of publication April 11, 2019; date of current version June 5, 2019. This work was supported in part by the U.K. Engineering and Physical Sciences Research Council (EPSRC) under Grant EP/N015924/1, in part by the U.K. Research Center in Non-Destructive Evaluation (RCNDE), in part by BAE Systems, in part by EDF Energy, in part by Hitachi, and in part by Wood Group (formerly, Amec Foster Wheeler U.K.). *(Corresponding author: Nicolas Budyn.)*

The authors are with the Department of Mechanical Engineering, University of Bristol, Bristol BS8 1TR, U.K. (e-mail: n.budyn@.bristol.ac.uk).

This paper has supplementary downloadable material available at http://ieeexplore.ieee.org, provided by the authors.

Digital Object Identifier 10.1109/TUFFC.2019.2909988

[1]The authors prefer the term *multiview* over *multimode* because the latter also refers to nondestructive inspections with different techniques (ultrasonic, eddy current, radiography testing, etc.).

This work is licensed under a Creative Commons Attribution 3.0 License. For more information, see http://creativecommons.org/licenses/by/3.0/

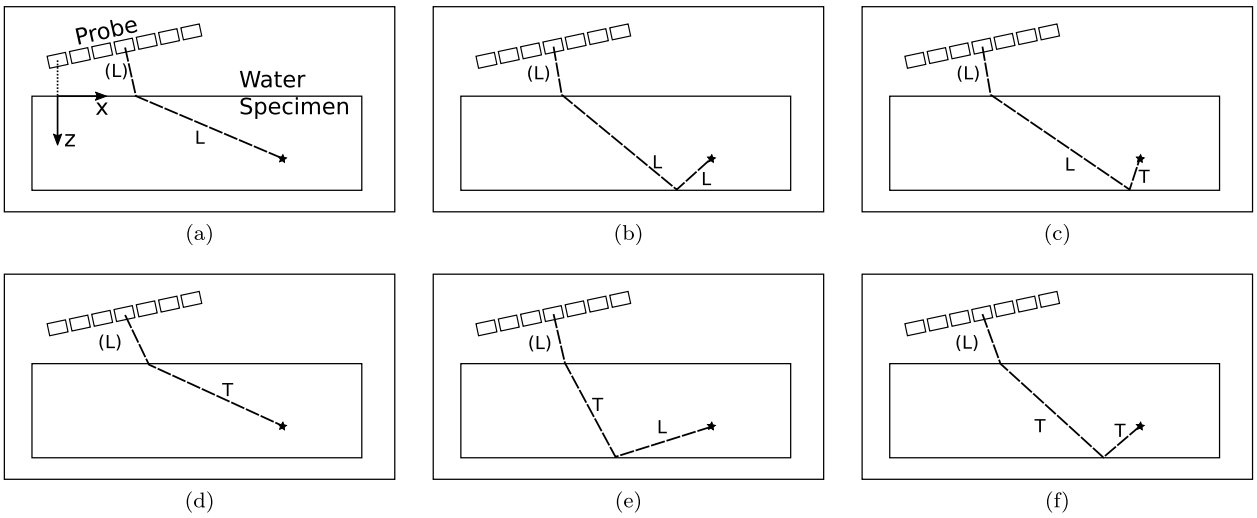

Fig. 1. Ray paths considered between an array element and an image point described using transmission nomenclature. (a) L. (b) LL. (c) LT. (d) T. (e) TL. (f) TT. In reception nomenclature, the modes are read from the image point instead of from the array. In both cases, the L mode in water is omitted from the path nomenclature for brevity.

below the array. Both the inspected object and the array are immersed in water. The specimen is a homogeneous isotropic metal block. The top and bottom surfaces (front and back walls) are planar.

B. Multiview Imaging

Multiview imaging considers various ray paths between the ultrasonic array and a grid of points to form multiple images of the same physical region of interest in the examination object. Fig. 1 shows the six paths considered in this paper, with zero or one internal reflection against the back wall and with longitudinal (L) and transverse (T) waves: L, T, LL, LT, TL, and TT. For conciseness, the L mode in water is not included in the description of the path as this is the only mode supported in a fluid. In the transmission nomenclature (transmitter–image point), the modes are read from the probe to the image point. In the reception nomenclature (image point–receiver), the modes are read from the image point to the probe. The full ray paths, transmitter–image point–receiver, are obtained by the combination of a transmit path and a receive path from these six. For example, the full path L–TL corresponds to the L path in transmission and TL path in reception (scattered T wave and mode conversion T to L against the back wall).

In multiview imaging, each full path is used to create a view. Because the FMC matrix is symmetrical due to the reciprocity of linear elastodynamics, algorithms based only on the times of flight, such as TFM, produce redundant views [17]. From these six paths, 21 views are unique out of a total of 36.

II. Model Description

A. Overview

The model predicts the scatterer response for every transmitter and receiver pair during the immersion inspection of a homogeneous isotropic object. This is an adaptation of the LTI model developed by Thompson and Gray [18] and Schmerr [19] to the multiview immersion inspection. The contribution of the scatterer to the time trace is calculated in three main steps: 1) the calculation of the incident wave amplitudes on the scatterer (transmit path); 2) the calculation of the scattering; and 3) the calculation of the wave amplitudes propagated back from the scatterer to the probe (receive path). The response of a scatterer located in the solid at point $\boldsymbol{y}$ (boldface is used to indicate vector quantities), insonified by the ith probe element and received by the jth element, is modeled

$$G_{ij}(\omega, \boldsymbol{y}) \coloneqq P_{ij}(\omega, \boldsymbol{y}) e^{\imath\omega \mathcal{T}_{ij}(\boldsymbol{y})} U(\omega) \tag{1}$$

with

$$P_{ij}(\omega, \boldsymbol{y}) \coloneqq T_i(\boldsymbol{y}) T'_j(\boldsymbol{y}) B_i(\boldsymbol{y}) B'_j(\boldsymbol{y}) D_i(\omega, \boldsymbol{y}) D'_j(\omega, \boldsymbol{y}) S_{ij}(\omega, \boldsymbol{y})$$

where:

1) $T_i(\boldsymbol{y})$ and $T'_j(\boldsymbol{y})$ encapsulate the real or complex plane wave transmission and reflection coefficients at the relevant fluid–solid interfaces encountered on, respectively, the transmit and receive paths [19];
2) $B_i(\boldsymbol{y})$ and $B'_j(\boldsymbol{y})$ describe the geometrical attenuation (beamspread) for, respectively, the transmit and receive paths;
3) $D_i(\omega, \boldsymbol{y})$ and $D'_j(\omega, \boldsymbol{y})$ are the directivity of the probe elements associated with the transmit and receive path directions in the couplant relative to the probe;
4) $S_{ij}(\omega, \boldsymbol{y})$ is the scattering amplitude;
5) $\mathcal{T}_{ij}(\boldsymbol{y})$ is the time of flight of the total ray path;
6) $U(\omega)$ is the ultrasonic toneburst.

Details about these terms are given in the following. Except $U(\omega)$, all these quantities are view-dependent. All elements are assumed to emit the same signal $U(\omega)$. The wave amplitudes are described by pressure in the fluid and displacement in the solid. The material attenuation in the samples considered in this paper is too low to give any significant difference, so it is ignored; it could, however, be accounted for if need be.

1) Scattering: Under the assumption that the incident wavefront is planar and of constant amplitude over the extent of

the defect (i.e., quasi-plane wave insonification), the defect response can be approximated by the infinite medium scattering amplitudes [18] [19, Sec. 10.1.1]. In other words, the inspection-specific calculation of the flaw response comes down to its calculation in the canonical case of a scatterer in an unbounded medium with an incident plane wave of unit amplitude. More specifically, the scattering amplitudes are defined as the ratio of the displacement of the scattered wave at an arbitrarily chosen reference distance divided by the displacement of the incident plane wave in an unbounded medium. For a given defect, they are functions of the frequency, the incident, and scattered angles.

This simplification has three main consequences. First, the abundant literature about flaw scattering in the unbounded case can be used. In particular, in this work, the scattering functions are obtained analytically for a side-drilled hole [20] and a crack (finite length, infinitesimal width) [21], and finite-element analysis can be employed for arbitrary shapes of defects such as notches (finite length and width) [22]. Second, it is possible to precompute and cache the scattering amplitudes for computational efficiency. Third, it is sufficient to calculate the rays between the array elements and only one point of the defect, typically its center. Practically, a defect is, therefore, modeled as a pointlike scatterer with a specific frequency-dependent angular amplitude distribution that depends on its type and size because their far-field scattering functions are the same.

2) Ray Tracing: Calculating the ray paths between the array elements and the scatterer is an essential step because all terms in (1) except $U(\omega)$ depend on the geometry of the rays. The rays are calculated using Fermat's minimum-time principle [23, Sec. 7.1.3.1]. Because the medium is made up of homogeneous layers, and because the rays in a homogeneous medium are straight, ray tracing is done by finding the points at the intersecting surfaces that minimize the time of flight, similar to the previous work [5]. For simplicity of implementation, the minimization is done numerically by discretizing the surfaces and considering all possible paths (brute-force approach).

The output of the ray-tracing step is the coordinates of the rays and their times of flight $\mathcal{T}_{ij}(\boldsymbol{y})$.

3) Directivity: Each element is modeled as a line-source piston (2-D equivalent of a rectangular piston), which leads to the following directivity function [1], [24]:

$$D(\omega, \boldsymbol{y}) = \operatorname{sinc} \frac{\pi a \sin\theta}{\lambda}$$

where θ is the angle between the normal of the element and the ray, a is the width of the probe element, and λ is the wavelength in the couplant.

4) Beamspread: The attenuation due to the beamspreading in an infinite medium and in two dimensions is $1/\sqrt{r}$. The beamspread through a planar interface can be rigorously calculated using a high-frequency approximation of the Rayleigh–Sommerfeld equation and the method of stationary phase [19, Sec. 8.3.1]. The ray theory method gives equivalent results [24, Sec. 2.5]. These functions are given in the Appendix.

5) Ultrasonic Toneburst: The ultrasonic toneburst $U(\omega)$ is the overall array response to a single reflector and encapsulates the input electrical signal and the transmit and receive dynamics of the acquisition instrument and the probe. This term is an input of the model; an experimental measurement technique to obtain it is described in [25].

In this work, $U(\omega)$ is modeled as the Fourier transform of a Hann-windowed sine wave scaled by a single coefficient measured experimentally.

6) Single-Frequency Approximation: The scatterer response defined in (1) is rewritten to separate the frequency-independent of the frequency-dependent terms

$$G_{ij}(\omega, \boldsymbol{y}) = P_{ij}(\omega_0, \boldsymbol{y}) Q_{ij}(\omega, \boldsymbol{y}) e^{\imath\omega\mathcal{T}_{ij}(\boldsymbol{y})} U(\omega) \tag{2}$$

with

$$Q_{ij}(\omega, \boldsymbol{y}) \coloneqq \frac{D_i(\omega, \boldsymbol{y}) D'_j(\omega, \boldsymbol{y}) S_{ij}(\omega, \boldsymbol{y})}{D_i(\omega_0, \boldsymbol{y}) D'_j(\omega_0, \boldsymbol{y}) S_{ij}(\omega_0, \boldsymbol{y})}$$

where ω_0 is the probe center frequency. To obtain the scatterer response, the toneburst is time-shifted, then rescaled and phase-shifted by the complex coefficient $P_{ij}(\omega_0, \boldsymbol{y})$, and finally, the shape and the amplitude of the toneburst are furthermore changed by the frequency-dependent coefficient $Q_{ij}(\omega, \boldsymbol{y})$. A first-order heuristic is to consider that the change in the response amplitude is mainly caused by $P_{ij}(\omega_0, \boldsymbol{y})$, whereas the frequency-dependent variation $Q_{ij}(\omega, \boldsymbol{y})$ causes a smaller amplitude variation in comparison. Ignoring this frequency dependence leads to the single-frequency approximation

$$G^{\omega_0}_{ij}(\omega, \boldsymbol{y}) \coloneqq P_{ij}(\omega_0, \boldsymbol{y}) e^{\imath\omega\mathcal{T}_{ij}(\boldsymbol{y})} U(\omega). \tag{3}$$

Under this approximation, the scatterer response is obtained by time-shifting and multiplying the toneburst by a single complex coefficient. The fine geometric features of the scatterer, conveyed in the frequency-dependent term, are lost. However, this single-frequency model may be useful when only a first-order amplitude estimation of the scatterer response is needed and is significantly faster to run than the multifrequency model.

B. Sensitivity Model for Predicting TFM Intensities

The time trace for the transmitter i and the receiver j is denoted $f_{ij}(t)$ in the time domain and $F_{ij}(\omega)$ in the frequency domain. Similarly, the simulated response to a single scatterer at position $\boldsymbol{y}$ is denoted $g_{ij}(t, \boldsymbol{y})$ and $G_{ij}(\omega, \boldsymbol{y})$. The analytic signals obtained using the Hilbert transform are denoted with a tilde: for example, $\tilde{f}_{ij}(t)$ and $\tilde{F}_{ij}(\omega)$.

For a given view, the TFM intensity at image point $\boldsymbol{r}$ is defined as

$$I_0(\boldsymbol{r}) \coloneqq \left| \sum_{i,j} a_{ij}(\boldsymbol{r}) \tilde{f}_{ij}(\mathcal{T}_{ij}(\boldsymbol{r})) \right| \tag{4}$$

where the times of flight, $\mathcal{T}_{ij}(\boldsymbol{r})$, and the arbitrary weights, $a_{ij}(\boldsymbol{r})$, are view-dependent. The weights $a_{ij}(\boldsymbol{r})$ can be used for spatial filtering [16], [26]; in the present work, uniform weighting is used ($a_{ij}(\boldsymbol{r}) = 1$).

In the vicinity of a scatterer, the TFM intensity $I_0(\boldsymbol{r})$ for a given view includes the scatterer response $g_{ij}(t, \boldsymbol{y})$ for this view (the desired signal) but may also include the scatterer response from other modes and wall echoes. These latter signals create artifacts in the images and interfere constructively or destructively with the desired scatterer response. However, because the times of arrival of the artifacts are, in general, different from those of the signals of interest, the artifacts are ignored here. Simulated artifact-free TFM images are obtained from the model by replacing the time trace $\tilde{f}_{ij}(t)$ by the scatterer response in the imaged view

$$I_1(\boldsymbol{r}, \boldsymbol{y}) \coloneqq \left| \sum_{i,j} a_{ij}(\boldsymbol{r}) \tilde{g}_{ij}(\mathcal{T}_{ij}(\boldsymbol{r}), \boldsymbol{y}) \right|. \tag{5}$$

For example, the artifact-free T–T image only contains the T–T defect response. The actual T–T image contains other defect echoes such as the L–L response and wall echoes; they are absent of the artifact-free image. To reduce the computational burden, the approximation defined in (3) is applied to obtain the single-frequency artifact-free image for a given view

$$I_2(\boldsymbol{r}, \boldsymbol{y}) \coloneqq \left| \sum_{i,j} a_{ij}(\boldsymbol{r}) \tilde{g}_{ij}^{\omega_0}(\mathcal{T}_{ij}(\boldsymbol{r}), \boldsymbol{y}) \right|. \tag{6}$$

Furthermore, only the intensity at a single point of the defect image, the defect center $\boldsymbol{y}$, is considered. For $\boldsymbol{r} = \boldsymbol{y}$, the TFM intensity becomes

$$\begin{aligned} I_2(\boldsymbol{r}, \boldsymbol{r}) &= \frac{1}{2\pi} \left| \sum_{i,j} a_{ij}(\boldsymbol{r}) \int_{-\infty}^{+\infty} \tilde{G}_{ij}^{\omega_0}(\omega, \boldsymbol{r}) e^{-\imath\omega\mathcal{T}_{ij}(\boldsymbol{r})}\, d\omega \right| \\ &= \frac{1}{\pi} \left| \sum_{i,j} a_{ij}(\boldsymbol{r}) \int_{0}^{+\infty} G_{ij}^{\omega_0}(\omega, \boldsymbol{r}) e^{-\imath\omega\mathcal{T}_{ij}(\boldsymbol{r})}\, d\omega \right| \\ &= \frac{1}{\pi} \left| \sum_{i,j} a_{ij}(\boldsymbol{r}) \int_{0}^{+\infty} P_{ij}(\omega_0, \boldsymbol{r}) U(\omega)\, d\omega \right|. \end{aligned} \tag{7}$$

Noting that $\frac{1}{\pi}\int_0^{+\infty} U(\omega)\, d\omega = \tilde{u}(0)$, the sensitivity image [17], [27] is defined as

$$E(\boldsymbol{r}) \coloneqq I_2(\boldsymbol{r}, \boldsymbol{r}) = \left| \tilde{u}(0) \sum_{i,j} a_{ij}(\boldsymbol{r}) P_{ij}(\omega_0, \boldsymbol{r}) \right|. \tag{8}$$

For a given view, the sensitivity image, $E(\boldsymbol{r})$, represents an estimate (under the single-frequency assumption) of the TFM intensity that would be measured if a defect of the prescribed type existed with its center at $\boldsymbol{r}$. The quality of the estimation is discussed in Section IV. This quantity requires less computation than the artifact-free TFM images $I_1(\boldsymbol{r}, \boldsymbol{y})$ and $I_2(\boldsymbol{r}, \boldsymbol{y})$ because: 1) no frequency integration is required and 2) the TFM algorithm is performed at a single point, the defect center, instead of on a grid in the vicinity of the defect. One may note that the exact form of the toneburst $U(\omega)$ is ignored in this sensitivity model because of the single-frequency assumption; only the amplitude of its envelope at $t = 0$, $|\tilde{u}(0)|$ matters and acts in practice as a scaling coefficient.

C. Time Interpolation of Time Traces in TFM

Numerically, the TFM is usually calculated in its time-domain form (4)–(6) where the time traces are linearly interpolated between time samples [4]. However, because of this linear interpolation, the intensities obtained with the time-domain forms are systematically lower than the ones obtained with the frequency-domain forms of TFM like (7) and (8). The magnitude of this difference depends on the sampling rate and frequency content of the signals and varies from pixel to pixel; at 25-MHz sampling rate with a nominal center frequency of 5 MHz, it was observed to be around 2 dB. In practice, linear interpolation is generally sufficient and a heuristic correction based on the sampling rate and the ultrasonic frequency could be applied if desired; however, in order to systematically eliminate the effect of this variation from subsequent comparisons, the more accurate Lanczos interpolation [28], [29] is used in this work

$$k(t) = \sum_{n=\lfloor t/T \rfloor - a + 1}^{\lfloor t/T \rfloor + a} k(nT) L(t/T - n) \tag{9}$$

where $1/T$ is the sampling frequency, and $L(x)$ is the Lanczos kernel of order b

$$L(x) = \begin{cases} \operatorname{sinc}(\pi x) \operatorname{sinc}(\pi x/a), & \text{if } -a < x < a \\ 0, & \text{otherwise.} \end{cases}$$

With a kernel of order $a = 3$, the error is reduced to 0.001 dB, at the cost of a ten-times slower computation of TFM images compared to linear interpolation (CPU implementation).

III. Multifrequency Model Validation

The multifrequency model defined previously is validated in this section against experimental data and data obtained from the FEM in three different cases described in Table I. The FEM data are generated using a 2-D hybrid model that couples: 1) a similar analytical model for the wave propagation in the fluid and 2) the Pogo solver [30] for modeling the elastic propagation and interaction inside the solid [31]. The nodes at the fluid/solid interfaces of this hybrid model act as Huygens sources for the pressure in fluid and for the vertical displacement in the solid. The material defined in the FEM simulation has the density and velocities of a copper–nickel alloy but has no material attenuation.

In the experimental data sets, each time trace is time-shifted by the instrument acquisition delay, measured by subtracting the times of arrival of two consecutive front-wall echoes in normal incidence, so that the maximum amplitude of the transmitted toneburst $\tilde{u}(t)$ is obtained at $t = 0$. The probe location is calculated from the times of arrival of the front-wall echo in the pulse-echo time traces. The longitudinal and transverse velocities in the sample material are obtained under the assumption that the correct values maximize the TFM intensities of the back-wall echo; the block thickness being known, the longitudinal and traverse velocities are thereby obtained from the L–L and L–T views, respectively.

The time traces (experimental, FEM, and simulated) are filtered with a fourth-order Butterworth bandpass filter to

TABLE I
DESCRIPTION OF THE THREE VALIDATION CASES

Dataset name	Crack	Notch	SDH
Source	FEM	Experiment	Experiment
Defect properties			
Type	crack	notch	SDH
Size	0.5 mm	3×1 mm	Ø1 mm
Orientation	110°	90° (vertical)	/
Location x (mm)	26	46	46
Location z (mm)	10	20	20
Block properties			
Material	copper nickel	aluminium	aluminium
L velocity (m/s)	5050	6384	6410
T velocity (m/s)	2534	3156	3150
L att. (Np/m)	0	0[1]	0[1]
T att. (Np/m)	0	0[1]	0[1]
Density (kg/m^3)	7800	2700[1]	2700[1]
Thickness (mm)	20	40	40
Probe properties			
Number of elements	110	64	64
Centre frequency (MHz)	5	2.5	2.5
Element pitch (mm)	0.17	0.5	0.5
Probe stand-off (mm)	17.0	29.9	29.8
Probe angle	11.0°	12.5°	12.5°
Filter passband (MHz)	2–8	1–4	1–4

[1] Not measured.

remove potential low-frequency offsets and high-frequency noise. The filter has a negligible impact on the toneburst bandwidth.

For the ray tracing, the distance between two consecutive points of the discretized interfaces is 30 μm. Compared to a twice as coarse grid, the largest observed difference of TFM defect intensities for the notch data set was 0.02 dB, which demonstrates that the interfaces are fine enough to make the error negligible.

To measure the model scaling coefficient $|\tilde{u}(0)|$, the back-wall reflection for the L–L path is modeled using a ray-based approach consistent to that described above for pointlike scatterers. The amplitudes of the back wall are measured by taking for each experimental/FEM time trace the maximum of the envelope of the signal near the expected time of arrival. The ratio between the modeled and experimental back-wall amplitudes is the model scaling; this ratio is assumed to be the same for all pairs of time traces. An ordinary least-squares regression is performed for robustness to obtain the final model coefficient. The back wall reflected for the path L–L was chosen because it provides a strong signal, clearly visible in all time traces. In [17], the front-wall reflection was used instead; however, the back wall appears to be less sensitive to small probe misalignments and, therefore, provides a more robust estimation of the model scaling. A proper investigation would require a 3-D model to understand the effect of the out-of-plane misalignment in the front- and back-wall amplitudes.

A. Results

Figs. 2 and 3 show the simulated and experimental/FEM defect response images in different views on a decibel scale; in each image, 0 dB corresponds to the maximum intensity in the magenta box. A good qualitative agreement is achieved: the tip diffraction and the specular reflection of the notch, and various defect patterns are generally correctly simulated.

Fig. 4 shows a quantitative absolute comparison of the maximum TFM intensities around the defect in experimental/FEM images $I_0(\boldsymbol{r})$ and simulated ones $I_1(\boldsymbol{r}, \boldsymbol{y})$. The measurement area is a square of side 5 mm (magenta squares in Figs. 2 and 3); the pixel size is 0.25 mm. Due to computational limitations, the simulation time of the FEM data is shorter than the times of arrival of the waves in some views; therefore, only 12 views are available for the crack data set. The median/standard deviation of the errors for all views are −1.7/2.4 dB (notch), 0.0/3.1 dB [side-drilled hole (SDH)], and 0.1/1.5 dB (crack). For 48 views out of 54, the agreement is within ±3 dB. The defect response varies significantly between the views: a variation of 20 dB (crack), 30 dB (notch), and 36 dB (SDH) is observed between the highest and lowest TFM intensities. These large variations are correctly explained by the model.

In views where the defect response is low (approximately less than −20 dB relative to the brightest view), the defect may be hard to distinguish from the surrounding artifacts because of their similar or stronger amplitudes. In this situation, the assumption that the measured amplitude is close to the artifact-free one becomes questionable.

IV. SENSITIVITY MODEL VALIDATION

The sensitivity model defined in (8) provides an estimate of the TFM intensity of a defect. To assess the validity of this estimation, Fig. 5 shows the absolute comparison of the sensitivity model amplitudes $E(\boldsymbol{r})$ against the maximum artifact-free multifrequency TFM images $I_1(\boldsymbol{r}, \boldsymbol{y})$ near the defect. The median/standard deviation of the errors for all views are 0.0/2.3 dB (notch), −0.1/2.3 dB (SDH), and −0.5/1.5 dB (crack). For 51 views out of 63, the agreement is within ±3 dB.

The sensitivity model assumes that the intensity at the defect center is a good estimate of the peak intensity. This assumption falls short when the intensity at the defect center is a trough due to a phase effect (for example, in Fig. 2(f), even though the estimate remains good in this case). The magnitude of this error between the sensitivity model and the multifrequency model depends on the view and the defect type and becomes stronger at higher frequencies. In the presented data sets, it appears particularly in the view LL-TT of the SDH. Despite this, a good agreement is achieved.

These results validate the single-frequency assumption (3): the peak TFM intensities are mainly explained by a single-frequency model; the multifrequency dependence of the model, including the scattering, has a limited effect in comparison. However, finer effects such as the tip diffraction require a proper multifrequency model; therefore, the images produced with the single-frequency model are not representative of the defects (images available in supporting data).

Fig. 6 shows the predicted TFM intensities of a notch anywhere and for any view; the configuration is the same as the notch data set described earlier except that 14 299 defect locations are considered. These sensitivity images exhibit large

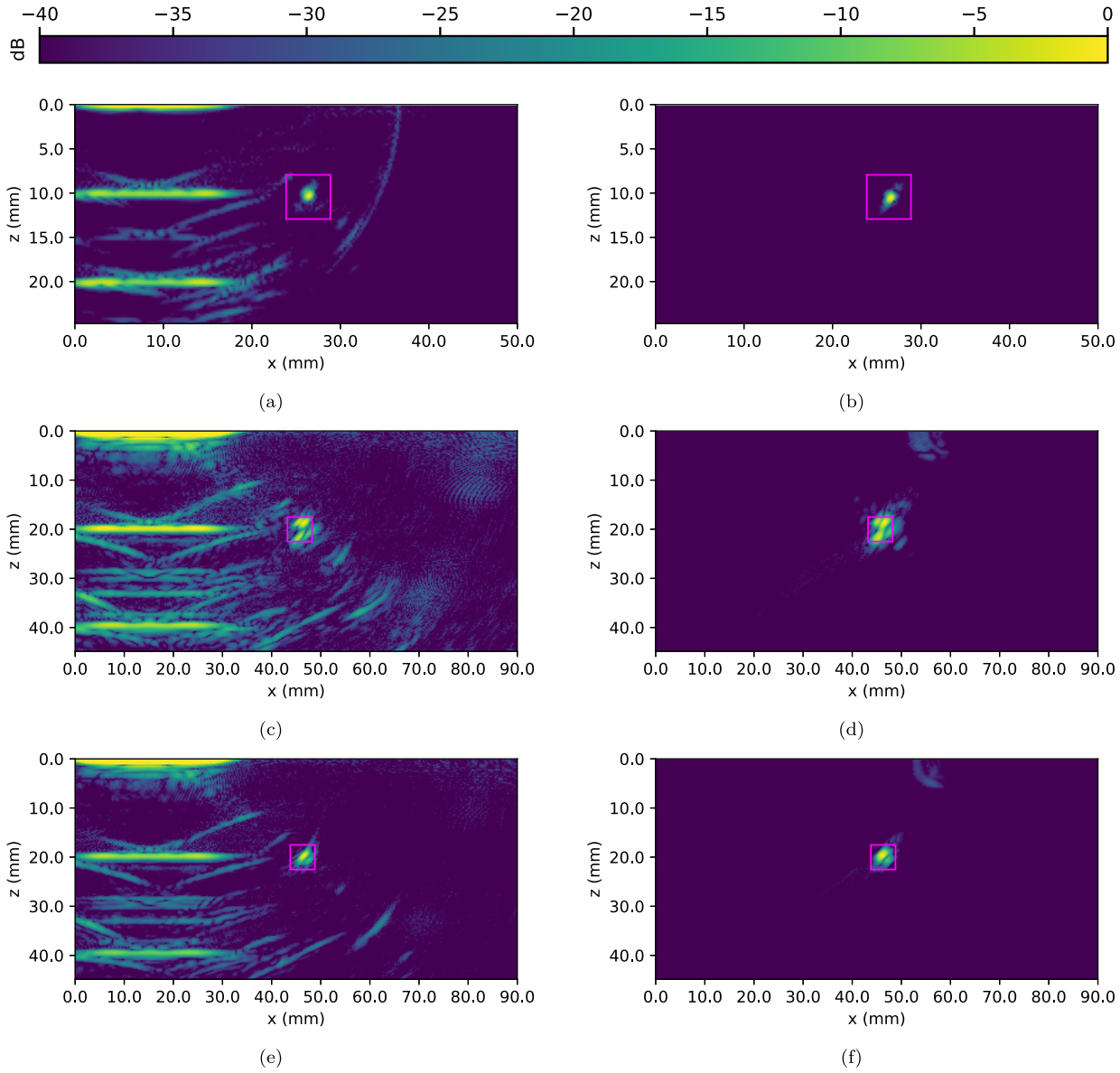

Fig. 2. TFM images of view T–T. Left column: experimental images $I_0(\boldsymbol{r})$. Right column: artifact-free simulated images $I_1(\boldsymbol{r}, \boldsymbol{y})$. Top row: crack. Middle row: notch. Bottom row: SDH. In each image, 0 dB corresponds to the maximum intensity in the magenta box.

variations of intensities, both within each view and across the views. They show clearly the areas of high intensities and the blind valleys, which are specific to the defect type and orientation. These images could be used to assess the suitability of an inspection configuration to detect a given defect. For example, the views L–L, LL-T, and TT–T seem particularly suited to inspecting a vertical notch at $x \approx 50$mm because they provide the highest TFM intensities and because they do not exhibit strong blind spots in this area.

The advantage of the sensitivity model is its high computational efficiency. The total runtime for these 14 299 defect locations, excluding the precalculation of the defect scattering distributions, which is performed in a first step and cached, is 75 s for 21 views on a desktop computer (Intel Core i7-4790 3.6 GHz quad-core processor; 16-GB RAM). To obtain equivalent results to the sensitivity model for 14 299 candidate defect locations, it would take 5 days using the artifact-free multifrequency model $I_1(\boldsymbol{r}, \boldsymbol{y})$ (30 s per location) and 39 years with the current finite-element analysis implementation (1 day per location). The sensitivity model is, therefore, three orders of magnitude faster than the multifrequency analytical model. This significant speedup is obtained because the sensitivity model provides only an *estimate* of the TFM intensity, under the single-frequency approximation and under the assumption that the intensity at the defect center is representative of the actual peak intensity.

Finally, instead of computing the TFM intensities of a given defect type and orientation at different positions, this fast model could also conversely be used to quickly predict the TFM intensities of different defect types and orientations at one position, as an input for defect characterization techniques. Its speed, flexibility, and relative accuracy are crucial benefits.

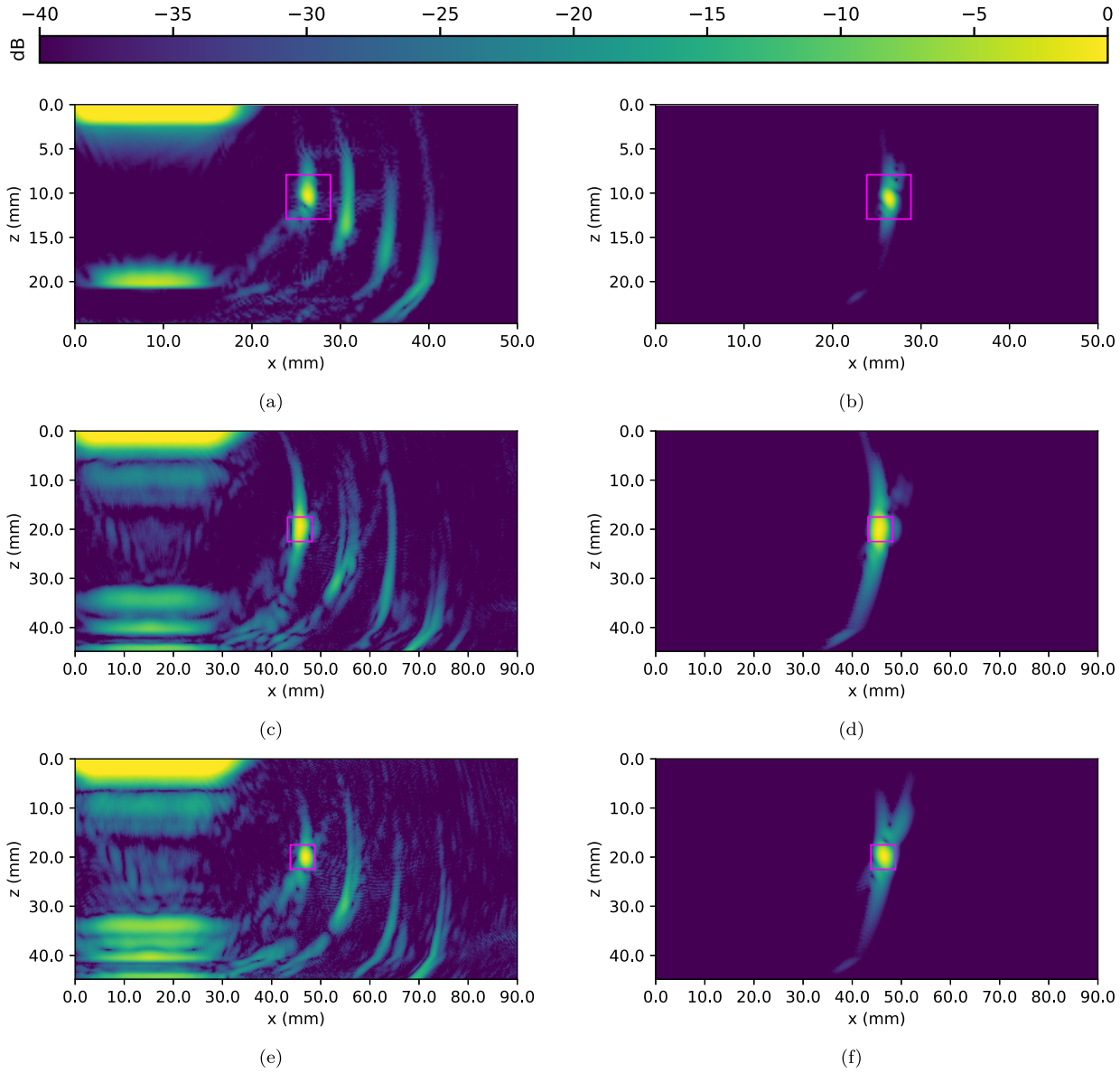

Fig. 3. TFM images of view LL–T. Left column: experimental images $I_0(\boldsymbol{r})$. Right column: artifact-free simulated images $I_1(\boldsymbol{r}, \boldsymbol{y})$. Top row: crack. Middle row: notch. Bottom row: SDH. In each image, 0 dB corresponds to the maximum intensity in the magenta box.

V. Conclusion

A 2-D ray-based forward model for small defects was described and compared against FEM and experimental data for the inspection of a side-drilled hole, a crack, and a notch. The model is used to predict artifact-free images of the defect. The model results are normalized against the measurements of the back-wall echo. The model agrees with the experimental/FEM data within typically ±3 dB. Under a single-frequency assumption and assuming the maximum TFM intensify of the defect is at located at its center, which is most often the case for small defects, a simpler model named the sensitivity model is derived. A typical ±3-dB agreement between this simple model and the fuller one is achieved. The sensitivity model is typically three orders of magnitude more computationally efficient and, therefore, is used to compute sensitivity images in less than 2 min, which are the predicted TFM intensities of a given defect in any view and anywhere. These images provide quantitative results to determine the views and the areas where a given defect type provide a large response. The sensitivity model was derived in this paper from a 2-D model but could be similarly obtained from a 3-D model; whether the agreement would remain acceptable has not been studied. In parallel work, the authors characterized the structural noise present in multiview TFM images [32]; this will be combined with the sensitivity model developed in the current paper to provide quantitative estimates of the signal-to-noise ratio for any defect at any location in any view. This is a key input into any future data-fusion algorithm for improved defect detection and characterization from multiview TFM images.

Appendix

A. Transmitter and Scatterer in the Same Medium

The beamspread coefficient for the transmit path between the ith element located at $\boldsymbol{x}_i$ and a scatterer located at $\boldsymbol{y}$ is

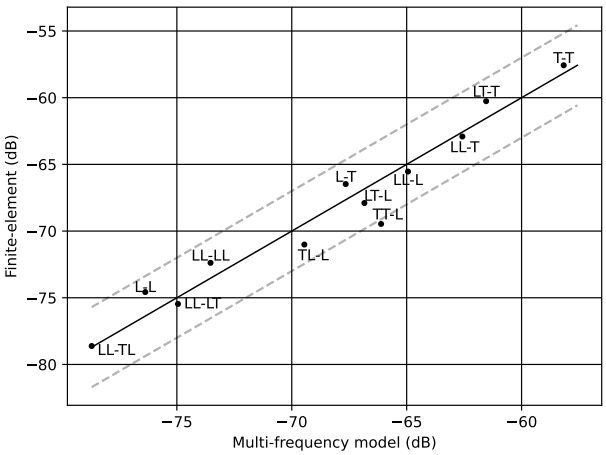

(a)

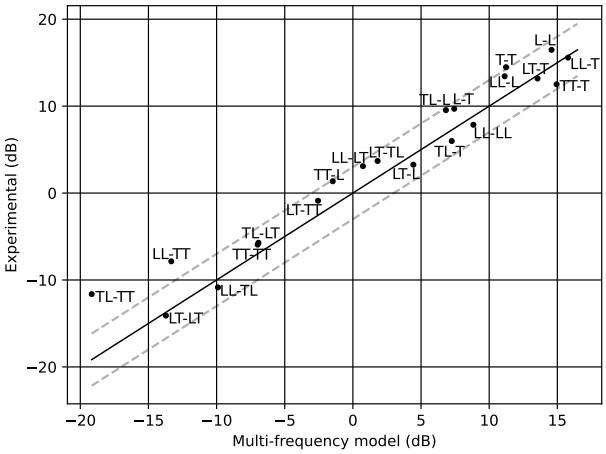

(b)

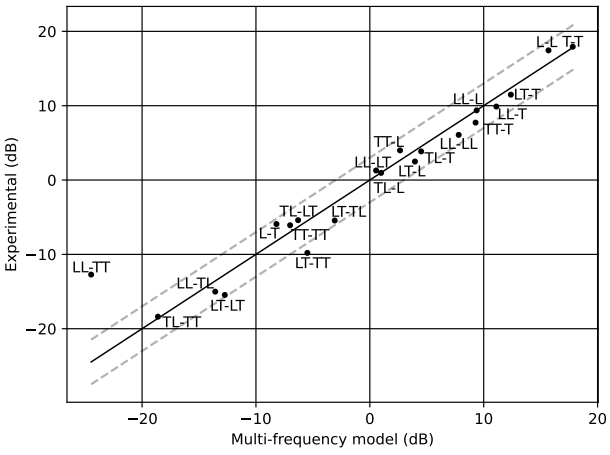

(c)

Fig. 4. Comparison of the peak intensity scatterer responses in artifact-free multifrequency images $I_1(\boldsymbol{r}, \boldsymbol{y})$ and experimental/FEM images $I_0(\boldsymbol{r})$ for (a) crack, (b) notch, and (c) SDH. Black solid line: perfect agreement. Dashed lines: agreement of ±3 dB. The 0-dB point is set arbitrarily.

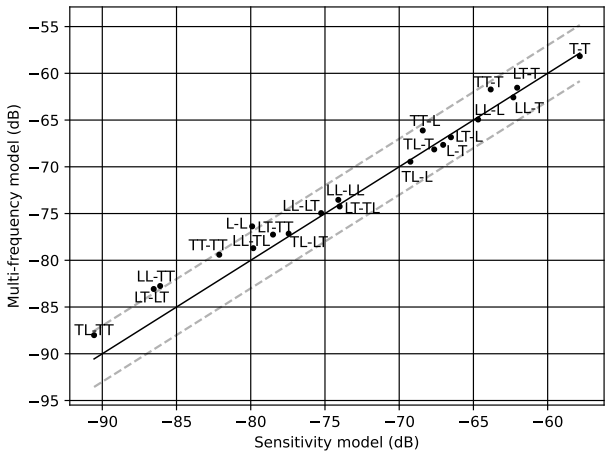

(a)

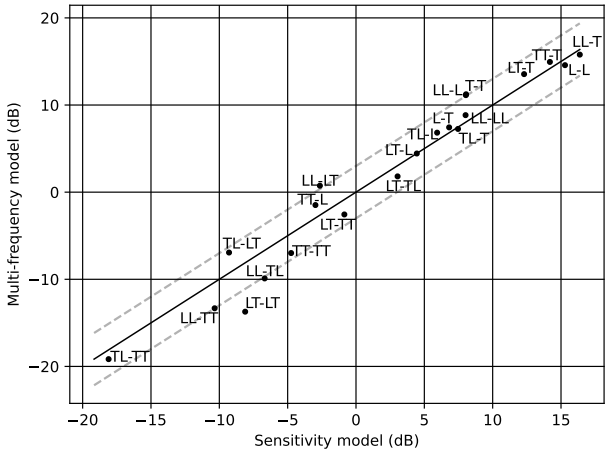

(b)

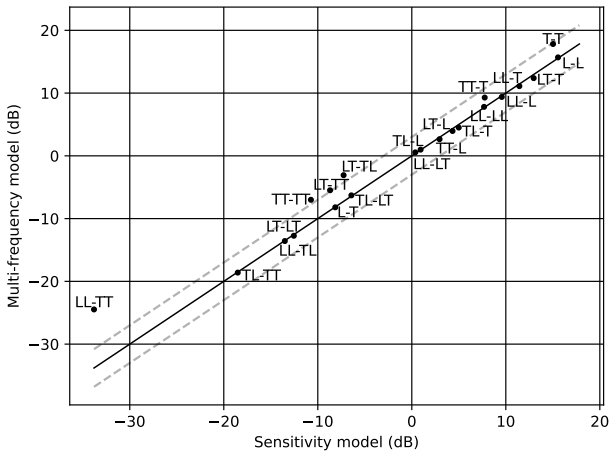

(c)

Fig. 5. Comparison of sensitivity image $E(\boldsymbol{r})$ and simulated multifrequency TFM image $I_1(\boldsymbol{r}, \boldsymbol{y})$ for (a) crack, (b) notch, and (c) SDH. The 0-dB point is set arbitrarily.

defined here as

$$B_i(\boldsymbol{y}) = \sqrt{\frac{1}{\|\boldsymbol{x}_i - \boldsymbol{y}\|}} \tag{10}$$

where $\|\cdot\|$ denotes the Euclidean distance. By symmetry the beamspread coefficient for the receive path, $B_i'(\boldsymbol{y})$, is the same.

B. Beamspread After One Transmission

We consider a first ray that starts from M_0 in medium 1, intersects the interface at the point M_1, and ends in M_2 in medium 2 after refraction [Fig. 7(a)]. The Snell–Descartes law states that

$$\frac{\sin \alpha_1}{\sin \beta_1} = \frac{c_1}{c_2}.$$

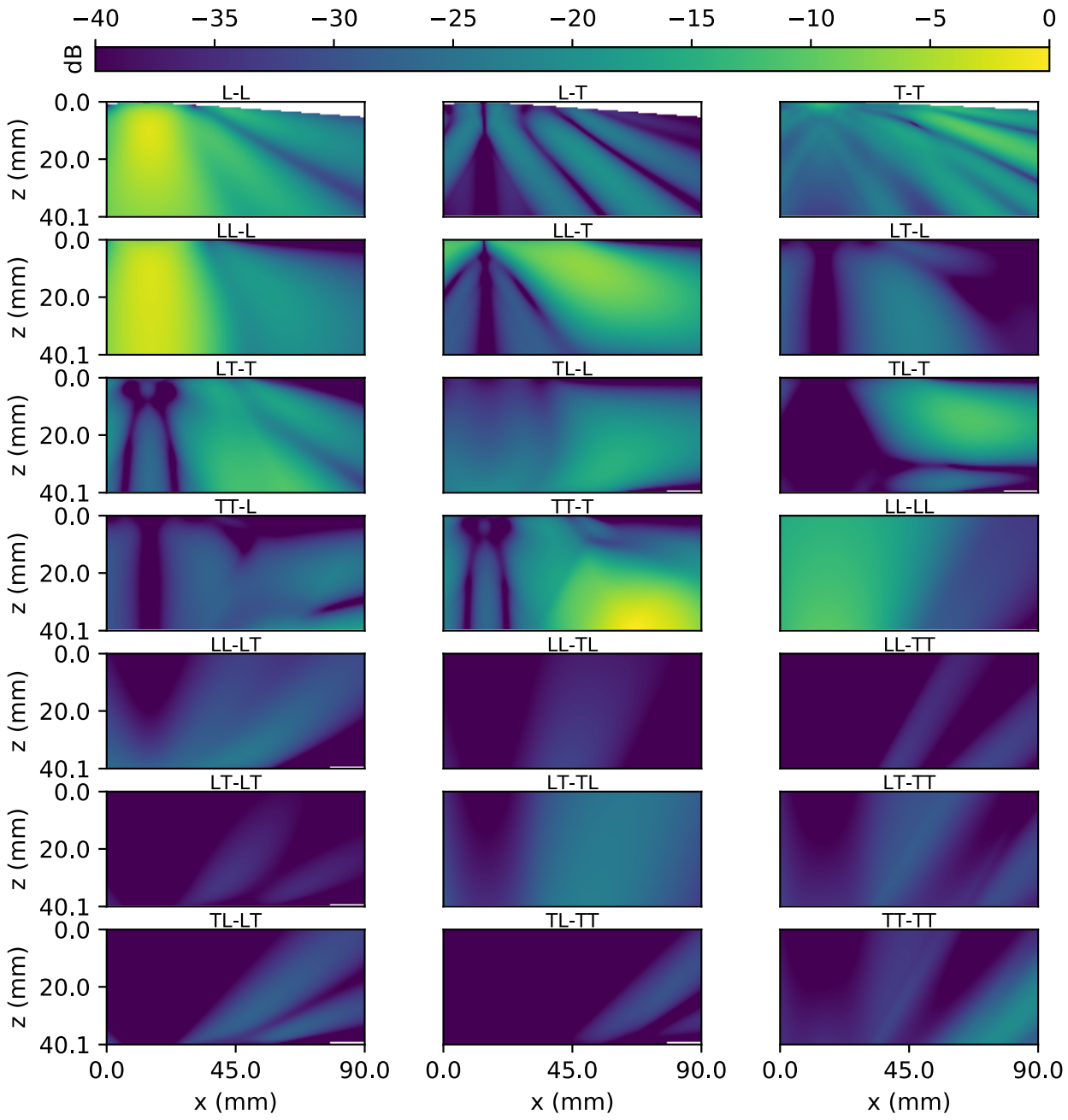

Fig. 6. Sensitivity images (dB) for a 3 mm × 1 mm vertical notch.

The quantity c_2 is either the longitudinal or the transverse wave speed in medium 2.

A second ray that leaves M_0 with an angle difference of $d\theta$ from the first ray intersects the interface at the point M_1'' and is also transmitted in medium 2 following the Snell–Descartes law. The beam that emerges in medium 2 from the segment M_1M_1'' appears to come from a virtual point source M_1'. Using a first-order approximation for small $d\theta$ and the Snell–Descartes law, it can be shown that [24, B.2]

$$\left|M_1'M_1\right| = \gamma_1 |M_0M_1|$$

where $|\cdot|$ denotes here the Euclidean distance between two points and where

$$\gamma_1 := \frac{c_1 \cos^2 \beta_1}{c_2 \cos^2 \alpha_1}.$$

The distance between the endpoint M_2 and the virtual source M_1' is, therefore,

$$\left|M_1'M_2\right| = \gamma_1 |M_0M_1| + |M_1M_2| = \gamma_1 |M_0M_1| + |M_1M_2|.$$

Conservation of energy dictates that the wave amplitude decreases in proportion to the square root of the separation

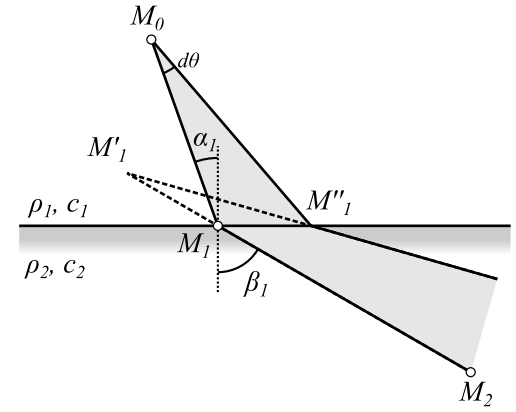

(a)

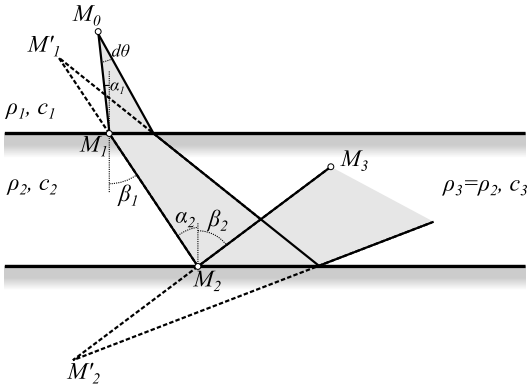

(b)

Fig. 7. (a) Beamspread after one interface. (b) Beamspread after two interfaces.

between the rays and hence in inverse proportion to the square root of the distance from the virtual source

$$B(M_2) = \sqrt{\frac{a}{\gamma_1|M_0M_1| + |M_1M_2|}}.$$

By continuity of the beamspread at the interface

$$\lim_{M_2\to M_1} B(M_2) = \lim_{|M_1M_2|\to 0} \sqrt{\frac{a}{\gamma_1|M_0M_1| + |M_1M_2|}} = \sqrt{\frac{a}{\gamma_1|M_0M_1|}}.$$

Also

$$\lim_{M_2\to M_1} B(M_2) = B(M_1) = \sqrt{\frac{1}{|M_0M_1|}}$$

so $a = \gamma_1$. This finally gives the beamspread coefficient after one transmission for the ray between the element $\boldsymbol{x}_i = M_0$ and the scatterer $\boldsymbol{y} = M_2$ is:

$$B_i(\boldsymbol{y}) = \sqrt{\frac{1}{|M_0M_1| + |M_1M_2|/\gamma_1}}. \tag{11}$$

By symmetry, the beamspread coefficient for the reverse path is

$$B'_i(\boldsymbol{y}) = \sqrt{\frac{1}{|M_1M_2| + |M_0M_1|/\gamma'_1}} = \sqrt{\frac{1}{|M_1M_2| + \gamma_1|M_0M_1|}} \tag{12}$$

where

$$\gamma'_1 \coloneqq \frac{c_2\cos^2\alpha_1}{c_1\cos^2\beta_1} = \frac{1}{\gamma_1}.$$

C. Beamspread After Multiple Transmissions or Reflections

The general expression for multiple interfaces can be found recursively from (11); the demonstration is left to the reader.

Extending the notations introduced earlier, α_k is the incident angle at the kth interface, β_k is the corresponding refracted/reflected angle, $\nu_k \coloneqq c_k/c_{k+1}$ is the kth refractive index, and γ_k is defined as

$$\gamma_k \coloneqq \nu_k\frac{\cos^2\beta_k}{\cos^2\alpha_k} = \frac{\nu_k\cos^2\beta_k}{1-\nu_k^2\sin^2\beta_k} = \frac{\nu_k^2 - \sin^2\alpha_k}{\nu_k\cos^2\alpha_k}.$$

For a n-legged ray ($n-1$ interfaces), the beamspread is

$$B_i(\boldsymbol{y}) = \left(\sum_{k=0}^{n-1}\frac{|M_kM_{k+1}|}{\prod_{l=1}^{k}\gamma_l}\right)^{-1/2} \tag{13}$$

where $\boldsymbol{x}_i = M_0$ is the center of the ith array element and the scatterer is $\boldsymbol{y} = M_n$.

ACKNOWLEDGMENT

The authors would like to thank Dr. A. Kashubin of Imperial College London for providing the finite-element method results for the crack. Data and code are available at the University of Bristol data repository, data.bris, at https://doi.org/10.5523/bris.2plergoban2sh2dhqy1q122e1d.

REFERENCES

[1] B. W. Drinkwater and P. D. Wilcox, "Ultrasonic arrays for non-destructive evaluation: A review," *NDT E Int.*, vol. 39, no. 7, pp. 525–541, Oct. 2006.
[2] H. Ammari *et al.*, *Mathematical and Statistical Methods for Multistatic Imaging*, vol. 2098. Cham: Springer, 2013.
[3] L. Borcea, G. Papanicolaou, C. Tsogka, and J. Berryman, "Imaging and time reversal in random media," *Inverse Problems*, vol. 18, no. 5, p. 1247, 2002.
[4] C. Holmes, B. W. Drinkwater, and P. D. Wilcox, "Post-processing of the full matrix of ultrasonic transmit-receive array data for non-destructive evaluation," *NDT E Int.*, vol. 38, no. 8, pp. 701–711, 2005.
[5] J. Zhang, B. W. Drinkwater, P. D. Wilcox, and A. J. Hunter, "Defect detection using ultrasonic arrays: The multi-mode total focusing method," *NDT E Int.*, vol. 43, no. 2, pp. 123–133, 2010.
[6] A. Fidahoussen, P. Calmon, M. Lambert, S. Paillard, and S. Chatillon, "Imaging of defects in several complex configurations by simulation-helped processing of ultrasonic array data," in *Proc. AIP Conf.*, vol. 1211, Feb. 2010, pp. 847–854.
[7] R. Long, J. Russell, and P. Cawley, "Ultrasonic phased array inspection using full matrix capture," *Insight-Non-Destructive Test. Condition Monitor.*, vol. 54, no. 7, pp. 380–385, Jul. 2012.

[8] Y. D. Zhang, X. Shen, R. Demirli, and M. G. Amin, "Ultrasonic flaw imaging via multipath exploitation," *Adv. Acoust. Vib.*, vol. 2012, Jan. 2012, Art. no. 874081.

[9] M. V. Felice, A. Velichko, and P. D. Wilcox, "Accurate depth measurement of small surface-breaking cracks using an ultrasonic array post-processing technique," *NDT E Int.*, vol. 68, pp. 105–112, Dec. 2014.

[10] A. Fidahoussen, "Développement d'une méthode de reconstruction ultrasonore pour la localisation et la caractérisation de défauts," Ph.D. dissertation, Univ. Paris-Sud, Orsay, France, Sep. 2012.

[11] S. Chatillon, S. Robert, P. Brédif, P. Calmon, G. Daniel, and F. Cartier, "Results of the 2014 UT modeling benchmark obtained with models implemented in CIVA: Solution of the FMC-TFM ultrasonic benchmark problem using CIVA," in *Proc. AIP Conf.*, Mar. 2015, vol. 1650, no. 1, pp. 1847–1855.

[12] J. Zhang, T. Barber, A. Nixon, and P. Wilcox, "Investigation into distinguishing between small volumetric and crack-like defects using multi-view total focusing method images," in *Proc. AIP Conf.*, Feb. 2017, vol. 1806, no. 1, p. 040003.

[13] F. Foroozan and S. ShahbazPanahi, "MUSIC-based array imaging in multi-modal ultrasonic non-destructive testing," in *Proc. IEEE 7th Sensor Array Multichannel Signal Process. Workshop (SAM)*, Jun. 2012, pp. 529–532.

[14] L. Le Jeune, S. Robert, E. L. Villaverde, and C. Prada, "Plane wave imaging for ultrasonic non-destructive testing: Generalization to multi-modal imaging," *Ultrasonics*, vol. 64, pp. 128–138, Jan. 2016.

[15] J. F. Cruza, J. Camacho, and C. Fritsch, "Plane-wave phase-coherence imaging for NDE," *NDT E Int.*, vol. 87, pp. 31–37, Apr. 2017.

[16] E. Iakovleva, S. Chatillon, P. Bredif, and S. Mahaut, "Multi-mode TFM imaging with artifacts filtering using CIVA UT forwards models," in *Proc. 10th Int. Conf. Barkhausen Noise Micromagnetic Test.*, vol. 1581, Feb. 2014, pp. 72–79.

[17] N. Budyn *et al.*, "Sensitivity images for multi-view ultrasonic array inspection," in *Proc. AIP Conf.*, Apr. 2018, vol. 1949, no. 1, p. 080001.

[18] R. B. Thompson and T. A. Gray, "A model relating ultrasonic scattering measurements through liquid–solid interfaces to unbounded medium scattering amplitudes," *J. Acoust. Soc. Amer.*, vol. 74, no. 4, pp. 1279–1290, Oct. 1983.

[19] L. W. Schmerr, Jr., *Fundamentals of Ultrasonic Nondestructive Evaluation: A Modeling Approach*, 2nd ed. New York, NY, USA: Springer, May 2016.

[20] A. L. Lopez-Sanchez, H.-J. Kim, L. W. Schmerr, Jr., and A. Sedov, "Measurement models and scattering models for predicting the ultrasonic pulse-echo response from side-drilled holes," *J. Nondestruct. Eval.*, vol. 24, no. 3, pp. 83–96, Sep. 2005.

[21] E. Glushkov, N. Glushkova, A. Ekhlakov, and E. Shapar, "An analytically based computer model for surface measurements in ultrasonic crack detection," *Wave Motion*, vol. 43, no. 6, pp. 458–473, 2006.

[22] A. Velichko and P. D. Wilcox, "A generalized approach for efficient finite element modeling of elastodynamic scattering in two and three dimensions," *J. Acoust. Soc. Amer.*, vol. 128, no. 3, pp. 1004–1014, Sep. 2010.

[23] A. Ben-Menahem and S. J. Singh, *Seismic Waves and Sources*. New York, NY, USA: Springer, 1981.

[24] L. W. Schmerr, Jr., *Fundamentals of Ultrasonic Phased Arrays* (Solid Mechanics and Its Applications), vol. 215. Cham, Switzerland: Springer, 2015.

[25] L. W. Schmerr, Jr., and S.-J. Song, *Ultrasonic Nondestructive Evaluation Systems*. Boston, MA, USA: Springer, 2007.

[26] C. Li, D. Pain, P. D. Wilcox, and B. W. Drinkwater, "Imaging composite material using ultrasonic arrays," *NDT E Int.*, vol. 53, no. 10, pp. 8–17, 2013.

[27] T. Stratoudaki, M. Clark, and P. D. Wilcox, "Laser induced ultrasonic phased array using full matrix capture data acquisition and total focusing method," *Opt. Express*, vol. 24, no. 19, pp. 21921–21938, Sep. 2016.

[28] C. E. Duchon, "Lanczos filtering in one and two dimensions," *J. Appl. Meteorol.*, vol. 18, no. 8, pp. 1016–1022, 1979.

[29] K. Turkowski, "Filters for common resampling tasks," in *Graphics Gems*. New York, NY, USA: Academic, 1990, pp. 147–165.

[30] P. Huthwaite, "Accelerated finite element elastodynamic simulations using the GPU," *J. Comput. Phys.*, vol. 257, pp. 687–707, Jan. 2014.

[31] A. Kashubin and P. Cawley, "Simulation of full matrix capture ultrasonic array data for immersion coupled inspection," submitted for publication.

[32] R. L. T. Bevan, J. Zhang, N. Budyn, A. J. Croxford, and P. D. Wilcox, "Experimental quantification of noise in linear ultrasonic imaging," *IEEE Trans. Ultrason., Ferroelectr., Freq. Control*, vol. 66, no. 1, pp. 79–90, Jan. 2018.

Nicolas Budyn was born in France in the early 1990s. He received the Engineer's (Diplôme d'ingénieur) degree from École Centrale de Nantes, Nantes, France, in 2015. He is currently pursuing the Ph.D. degree in engineering with the Ultrasonics and Nondestructive Testing Group, University of Bristol, Bristol, U.K., and BAE Systems, U.K.

From 2012 to 2015, he was a Trainee Engineer in nondestructive testing simulation in Framatome, Chalon-sur-Saône, France. His current research interests include ultrasonic array imaging and defect characterization.

Rhodri L. T. Bevan received the M.Eng. degree in civil engineering, the M.Res. degree in computational engineering, and the Ph.D. degree from Swansea University, Swansea, U.K., in 2005, 2006, and 2011, respectively.

From 2011 to 2013, he was a Research Assistant in the Civil and Computational Engineering Centre at Swansea University developing high-performance finite-element programs. From 2013 to 2016, he was a Research Assistant in numeric simulation and optimization in the Department of Aerospace Engineering at the University of Bristol, Bristol, U.K. Since 2016, he has been with the Department of Mechanical Engineering at the University of Bristol. His current research interests include array imaging, data fusion, and high-performance algorithm design.

Jie Zhang was born in Baoji, China, in 1975. He received the B.Eng., M.Eng., and Ph.D. degrees in instrument science and technology from the Harbin Institute of Technology (HIT), Harbin, China, in 1997, 1999, and 2002, respectively.

From 2002 to 2003, he was employed as a Research Fellow with the University of Warwick, Coventry, U.K. Since 2003, he has been a Research Associate with the University of Bristol, Bristol, U.K. His current research interests are focused on ultrasonic nondestructive evaluation (NDE) of layers, interfaces, ultrasonic wave scattering, and adaptive array imaging.

Anthony J. Croxford was born in Hatfield, U.K., in 1979. He received the M.Eng. degree in mechanical engineering and the Ph.D. degree from the University of Bristol, Bristol, U.K., in 2002 and 2005, respectively.

From 2005 to 2007, he was a Research Associate in the Nondestructive Testing Research Group at the University of Bristol, where he worked on the development of guided-wave structural health monitoring for permanently attached sensing systems. Since 2007, he has been a Lecturer in the Department of Mechanical Engineering at the University of Bristol. His current research interests include structural health monitoring, nonlinear ultrasonic techniques, and fluidized bed dynamics.

Paul D. Wilcox was born in Nottingham, U.K., in 1971. He received the M.Eng. degree in engineering science from the University of Oxford, Oxford, U.K., in 1994, and the Ph.D. degree from Imperial College London, London, U.K., in 1998.

He remained in the Non-Destructive Testing (NDT) Research Group at Imperial College London as a Research Associate until 2002, working on the development of guided-wave array transducers for large-area inspection. Since 2002, he has been with the Department of Mechanical Engineering at the University of Bristol, Bristol, U.K., where his current title is Professor of dynamics. He held an EPSRC Advanced Research Fellowship in Quantitative Structural Health Monitoring from 2007 to 2012, was the Head of the Mechanical Engineering Department from 2015 to 2018, and has been a fellow of the Alan Turing Institute for Data Science, London, U.K., since 2018. In 2015, he was a Co-Founder of Inductosense Ltd., Bristol, a spin-out company that is commercializing inductively coupled embedded ultrasonic sensors. His research interests include array transducers, embedded sensors, ultrasonic particle manipulation, long-range guided-wave inspection, structural health monitoring, elastodynamic scattering, and signal processing.